Materials Today Advances 21 (2024) 100476

Contents lists available at ScienceDirect

Materials Today Advances

journal homepage: www.journals.elsevier.com/materials-today-advances/

Irreversible pressure effect on phase transitions and bandgap narrowing of layered MoO_3

Shixia Wang [a,**], Yalin Wang [a], Tao Liu [a], Lu Wang [b], Yuxuan Huang [a], Yang Lu [c,d,*]

[a] Department of Chemistry, University of Shanghai for Science and Technology, Shanghai 200093, China
[b] School of Physical Science and Technology, ShanghaiTech University, Shanghai 201210, China
[c] Center for High Pressure Science and Technology Advanced Research, Shanghai 201203, China
[d] Shanghai Key Laboratory of Material Frontiers Research in Extreme Environments (MFree), Shanghai Advanced Research in Physical Sciences (SHARPS), Pudong, Shanghai 201203, China

A B S T R A C T

Two-dimensional layered molybdenum trioxide (MoO_3) holds significant importance in optoelectronics owing to its unique anisotropic structure and optical properties. Given that changes in structure can profoundly impact physical characteristics, it becomes imperative to explore new properties by means of acquiring different structures. Here, we report the irreversibility of structural evolution and optical properties of molybdenum trioxide under high pressure. The quenched MoO_3 possesses a stable high-pressure phase MoO_3-II, a narrowed bandgap (reduced by ~25%) and a strong optical absorption at visible to infrared region compared to the initial low-pressure phase α-MoO_3. These findings will facilitate the exploring of high-pressure phase materials under ambient conditions.

1. Introduction

Recently, there has been extensive research on two-dimensional (2D) materials with in-plane anisotropy. These materials include transition metal chalcogenides, group-VA, black phosphorus, and compounds consisting of two group-VA elements [1–9]. Some of these materials show significant potential for optoelectronic applications [10–12]. Molybdenum trioxide, among the available anisotropic 2D materials, is a wide bandgap semiconductor that exhibits quasi-transparency in the visible spectrum while maintaining electrical conductivity. This material has demonstrated its utility in various applications, including resistive memory technology, photovoltaics [13–15], electro-chromics [16], birefringence [17]and flexibility electronics [18]. Due to the discrepancy in the in-plane lattice parameters, α-MoO_3 exhibits an intrinsic suitability for investigating optical, mechanical, and electrical anisotropy within the plane. Notably, computational analyses have revealed the pronounced anisotropic nature of in-plane carrier mobility [19], and recent observations have demonstrated a remarkably anisotropic propagation of phonon polaritons in α-MoO_3 [20–24]. In contrast to metal plasma polaritons, phonon polaritons offer advantages such as reduced lower optical losses, improved optical confinement, and higher quality factors [25–29]. These intriguing optical properties are primarily arise from the anisotropy of the fundamental characteristics of molybdenum trioxide. As a van der Waals (vdW) layered material, molybdenum trioxide exhibits numerous unique properties. vdW structures provide a platform for designing quantum materials through the manipulation of weakly bonded atomic layers via twisting and stacking methods [22,30–32]. vdW materials with a small twist angle δ can be used to tune the electronic [33], magnetic, optical and mechanical properties of heterostructures [34,35]. Configurable coupling between phonon polaritons and lattice vibrations can be achieved in plates of twisted α-phase molybdenum trioxide (α-MoO_3) [21,36]. In contrast to other diffuse polaritons, the phonon polariton wavefront geometry as well as compressive and stretching deformations can be achieved in α-MoO_3 by simply changing δ. Twisted α-MoO_3 is expected to generate tunable infrared nano-light for various nanophotonic functions.

Other structures of molybdenum trioxide, particularly the high-pressure phase (MoO_3-II), have also received increasing attention due to their layered structure with strong anisotropy. As compared to α-MoO_3, MoO_3-II has a higher packing efficiency [39]. Similar to α-MoO_3, the color and electrical conductivity of MoO_3-II can be altered by the insertion of different ions, and MoO_3-II should have promising properties and applications, such as field effect transistors, optoelectronic devices, and energy storage devices [41]. On the other hand, the strong interlayer interactions between anisotropic 2D materials (e.g.,

* Corresponding author. Center for High Pressure Science and Technology Advanced Research, Shanghai, 201203, China.
** Corresponding author.
E-mail addresses: wangshixia@usst.edu.cn (S. Wang), yang.lu@hpstar.ac.cn (Y. Lu).

https://doi.org/10.1016/j.mtadv.2024.100476
Received 16 December 2023; Received in revised form 5 February 2024; Accepted 17 February 2024

α-MoO_3, black phosphorus) and symmetric 2D materials (e.g., graphene, transition metal chalcogenides) can result in in-plane anisotropy of symmetric 2D materials [42,44], thereby enabling the modulation of crystal orientation–dependent properties in 2D materials. However, there is limited research on this topic using MoO_3-II. The unique properties of MoO_3-II, apart from anisotropy, remain poorly understood, suggesting potential areas for future investigation.

This paper investigates the impact of pressure on the crystal structure of MoO_3 using Raman spectroscopy and X-ray diffraction. The results indicate that α-MoO_3 undergoes a structural phase transition to MoO_3-II at a pressure of 10 GPa at room temperature. Furthermore, another phase transition to MoO_3-III occurs above 25 GPa. Upon decompression, the crystal structure irreversibly reverts back to MoO_3-II. Additionally, the sample was subjected to multiple cycles of pressure up to a maximum pressure of 29.5 GPa, and the UV–Vis absorption spectra of α-MoO_3 were measured. Unusual changes were observed in the absorption spectra of the samples during the process. During the first compression, the absorption edge moves from 450 nm to 550 nm, indicating a significant increase in absorption of visible light. After decompression, a "bulge" from 700 nm to 800 nm appeared, signifying an increase in the infrared absorption of MoO_3-II. This before-decompression "bulge" at 700 nm–800 nm can be quenched to ambient pressure, showing the abnormal absorption changes resulting from the structural phase transition. However, during the second cycle of compression, the absorption of the sample did not exhibit significant changes throughout the process. Combining these observations with the Raman spectra and first-principle calculations suggests the pressure-induced structural irreversibility and optical variations.

2. Experimental and computational section

2.1. High-pressure Raman measurements

The commercial MoO_3 powder (99.99%) was used as the starting material. The structure of the powder was determined to be orthogonal, corresponding to α-MoO_3 (*Pnma*), by transmission electron microscopy (TEM). The starting MoO_3 powder was loaded into a Mao–Bell type symmetric diamond anvil cell (DAC, 300 μm culets). T301 stainless steel foil was pre-indented and a hole was laser drilled at the indentation center to serve as the gasket and sample chamber. Silicone oil was used as the pressure-transmitting medium (PTM) and the pressure was calibrated by measuring the frequency shift of the ruby R_1 fluorescence line [45]. Please note that silicone oil can provide a hydrostatic environment at pressure below ~6 GPa. High-pressure Raman spectroscopy measurement was conducted using the LabRAM HR evolutionary Raman system. The excitation wavelength was 532 nm. The spectral range spans from 50 to 2100 nm, with a spectral resolution better than 0.4 cm^{-1}.

2.2. Synchrotron X-ray diffraction

To prepare the quenched MoO_3, the starting MoO_3 powder was loaded into a DAC without pressure-transmitting medium (PTM), then, was compressed up to ~30 GPa and decompressed to ambient pressure. X-ray diffraction (XRD) experiments of samples were carried out at beamlines 15U1 (15U1A and 15U1B) and 17B of Shanghai Synchrotron Radiation Facility (SSRF). The integration and Rietveld refinement of XRD data were performed using the General Structure and Analysis System II (GSAS-II).

2.3. High-pressure optical absorption spectroscopy

The powder was pressed into a transparent platelet with the thickness of ~8 μm using a DAC [46]. Then, the sample was transferred into a DAC. Silicone oil was used as PTM. *In-situ* high pressure optical absorption spectroscopy measurements were conducted on a home-made UV–Vis spectroscopy system. During the measurement, the blank area near the sample was utilized as the reference area.

2.4. Computational details

The first-principles calculations in this study were performed using VASP software. To optimize the structural, α-MoO_3 and MoO_3-II were sampled in the Brillouin zone using Monkhorst-Pack grids with K-point densities of $2 \times 9 \times 8$ and $9 \times 9 \times 5$, respectively. The exchange-correlation interactions were treated using the generalized gradient approximation (GGA) proposed by Perdew, Burke, and Ernzerhof (PBE) [47], along with the inclusion of the DFT-D3 function [48] for van der Waals (vdw) correction. The atomic positions were relaxed until the maximum force on each atom was below 0.01 eV/Å. The energy cutoff of the plane wave was set to 650 eV, and the energy convergence criterion was set to 10^{-5} eV. The electronic properties for the optimized structure are computed using different K-point densities: 4x14x13 and 14x14x8. The resulting electronic properties are processed using the VASPKIT software package [49], which has been verified for accuracy and validity in numerous previous studies [50–52].

3. Results and discussion

3.1. Structural properties of orthorhombic and monoclinic MoO_3

Fig. 1a schematically displays the irreversibly pressure-induced phase transition from α-MoO_3 (*Pnma*) to MoO_3-II ($P2_1/m$). At ambient conditions, α-MoO_3 is an orthorhombic structure with *Pnma* space group with the lattice constants a = 13.822 Å, b = 3.695 Å, c = 3.952 Å, α = β = γ = 90° [53], and MoO_3-II is a monoclinic structure with $P2_1/m$ space group with lattice constants a = 3.954 Å, b = 3.687 Å, c = 7.095 Å, α = γ = 90°, β = 103.745° [54]. The orthogonal α-MoO_3 consists of MoO_6 octahedra with (ABA) stacking, while the monoclinic MoO_3-II exhibits (AAA) stacking. Compared to α-MoO_3, MoO_3-II has a higher stacking efficiency and reduced structural symmetry. The pressure-driven phase transition is realized by the mutual sliding or displacement motion of the molybdenum atoms in each layer along the *c*-axis. Fig. 1b presents the low-resolution TEM image of the starting sample viewed from the out-of-plane direction. The high-resolution TEM image and the corresponding selected area electron diffraction (SAED) confirm that the starting sample has a well-defined orthorhombic crystalline pattern and the anisotropic in-plane structure, corresponding to α-MoO_3.

The structural information of MoO_3 under high pressure has been investigated by high-pressure XRD and refinements in previous works [53,55], but the irreversibility of the phase transition remains unclear. Here, to determine the crystal structure or phase fraction of MoO_3 after pressure treatment, the XRD data of the recovered MoO_3 sample (from ~30 GPa to 0 GPa) was refined (see Fig. 1c). The Rietveld refinement suggests that the quenched sample is mainly dominated by the MoO_3-II phase, and merely contains a small amount of the starting α-MoO_3 phase (~5.5 wt%), which may be due to the presence of fine grains or the residual strain/shear (the sample was prepared under non-hydrostatic pressure). Fig. S1 shows the Raman spectra of the starting and quenched samples at ambient pressure. There are differences in the Raman peaks at less than 230 cm^{-1}, agreeing with the irreversibility of the phase transition. The processes of the pressure-induced phase transition will be discussed in detail below.

3.2. Structural evolution of MoO_3 under pressure

α-MoO_3 belongs to the D_{2h}^{16} point group and the vibrational modes can be expressed as follows [53]: $\Gamma = 8A_g+8B_{1g}+4B_{3g}+4A_u+3B_{1u}+7B_{2u}+7B_{3u}$, where A_g, B_{1g}, B_{2g} and B_{3g} correspond to Raman active modes, B_{1u}, B_{2u} and B_{3u} correspond to infrared active modes, and A_u mode is an inactive mode. Fig. 2a shows the change in Raman spectra during compression from ambient pressure

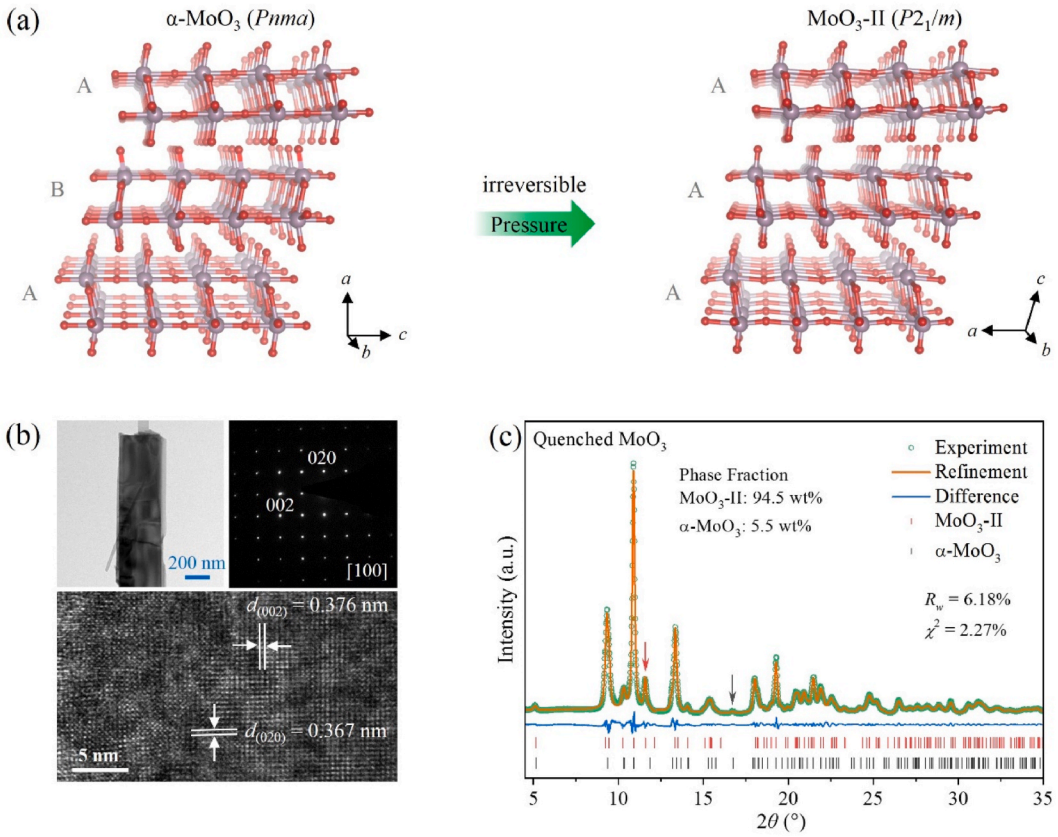

Fig. 1. Scheme of the irreversibly pressure-induced phase transition of trilayer α-MoO_3 (*Pnma*) to trilayer MoO_3-II ($P2_1/m$). (b) Low-resolution TEM image, selected area electron diffraction (SAED), and high-resolution TEM image of the starting α-MoO_3 sample. (c) Rietveld refinement of the XRD pattern (λ = 0.6199 Å) of the pressure-quenched MoO_3. Down arrows denote the characteristic peaks of phases.

to 29 GPa. At ambient pressure, the Raman peaks of MoO_3 are mainly distributed below 200 cm^{-1}, 200-500 cm^{-1}, and 600-1000 cm^{-1}. Among these peaks, 115 cm^{-1} and 127 cm^{-1} correspond to the translationally rigid B_{2g} and B_{3g} modes, respectively. The A_g peak at 157 cm^{-1} corresponds to the δ(O_2Mo_2)n mode. The peaks at 197 cm^{-1}, 217 cm^{-1}, and 244 cm^{-1} are due to the shearing of the δO_2-Mo-O_2 bond, which corresponds to the B_{2g}, A_g, and B_{3g} modes, respectively. The B_{2g} mode at 278 cm^{-1} is generated due to δO_1 = Mo═O_1 oscillations, and the B_{3g} mode at 335 cm^{-1} is generated by δO_3-Mo-O_3 deformation. The peaks at 364 cm^{-1} and 378 cm^{-1} are A_g and B_{1g} modes corresponding to δO_2 = Mo═O_2 shear, and the two peaks at 471 cm^{-1} and 665 cm^{-1} are, respectively, antisymmetric A_g and B_{2g} modes of δMo-O_2-Mo stretching vibrations. The strongest peak at 819 cm^{-1} corresponds to the A_g mode of stretching vibrations, and the A_g mode at 996 cm^{-1} is generated by the antisymmetric Mo═O_1 stretching vibrations [53,56,57].

During the compression from ambient pressure to 10 GPa, all the Raman peaks move to higher wave numbers regularly with little change in the peak intensities, indicating that the structure of α-MoO_3 remains stable up to 10 GPa. With increasing pressure above 10.2 GPa, a new Raman peak appears at 275 cm^{-1} and increases in intensity. Meanwhile, some of the Raman peaks in the low-frequency region gradually disappear (217 cm^{-1}, 335 cm^{-1} and 364 cm^{-1}). This phenomenon is attributed to a significant change in the O_2–Mo–O_2 angle, indicating a phase transition from orthorhombic α-MoO_3 to the structure of monoclinic MoO_3-II. The high-pressure phase exhibits stability until reaching ~25 GPa. When the pressure exceeded 25 GPa, the peaks at 389 cm^{-1}, 414 cm^{-1}, 510 cm^{-1}, and 737 cm^{-1} disappear, and two new Raman peaks appear at 826 cm^{-1} and 897 cm^{-1}. These new Raman peaks persists until 29 GPa, suggesting the onset of the second high-pressure phase MoO_3-III (or denoted as β-MoO_3). As shown in Fig. S2, MoO_3-III is no longer layered, where the MoO_6 octahedra share only corners with each other and each oxygen atom is shared by two octahedra. Fig. 2b shows the trend of each Raman mode with pressure and the discontinuous changes at around 10 GPa and 25 GPa, marked by two dashed lines, corresponding to the two phase transitions. After the pressure released to ambient pressure, the Raman peaks shift towards low wavenumber and finally the high-pressure phase MoO_3-II was prepared (Fig. 2a, Fig. S1, and Fig. S3a).

To further examine the high-pressure stability of MoO_3-II, we conducted a subsequent compression and decompression of the quenched samples and analyzed the *in-situ* Raman spectra up to 14 GPa (Fig. 2c and d, and Fig. S3b). The results reveal a gradual shift of the Raman modes towards higher wavenumbers as the pressure increased, without discontinuous change, suggesting the good stability of MoO_3-II at 0–14 GPa. Tables S1 and S2 summarized the slope values (dν/dp) of Raman modes of the starting and quenched samples with different high-pressure structures. We can find that the slope values of most modes (e.g., the main peak) of the starting sample are larger than that of the quenched sample, suggesting that the high-pressure phase MoO_3-II is more difficult to be compressed, as compared to the low-pressure phase α-MoO_3 [53].

3.3. *Optical variation of MoO_3 at high pressure*

Due to valence electron transitions induced by the absorption of UV or visible light, leading to alterations in UV–visible absorption, we conducted two in situ high-pressure UV–visible characterizations of the powder samples to investigate the impact of pressure on their optical absorption characteristic. Fig. 3a demonstrates that after the initial pressure treatment of the sample, we found that the absorption value of the sample gradually increased with the increase of pressure, and the optical absorption at 500 nm of the sample was obviously strengthened

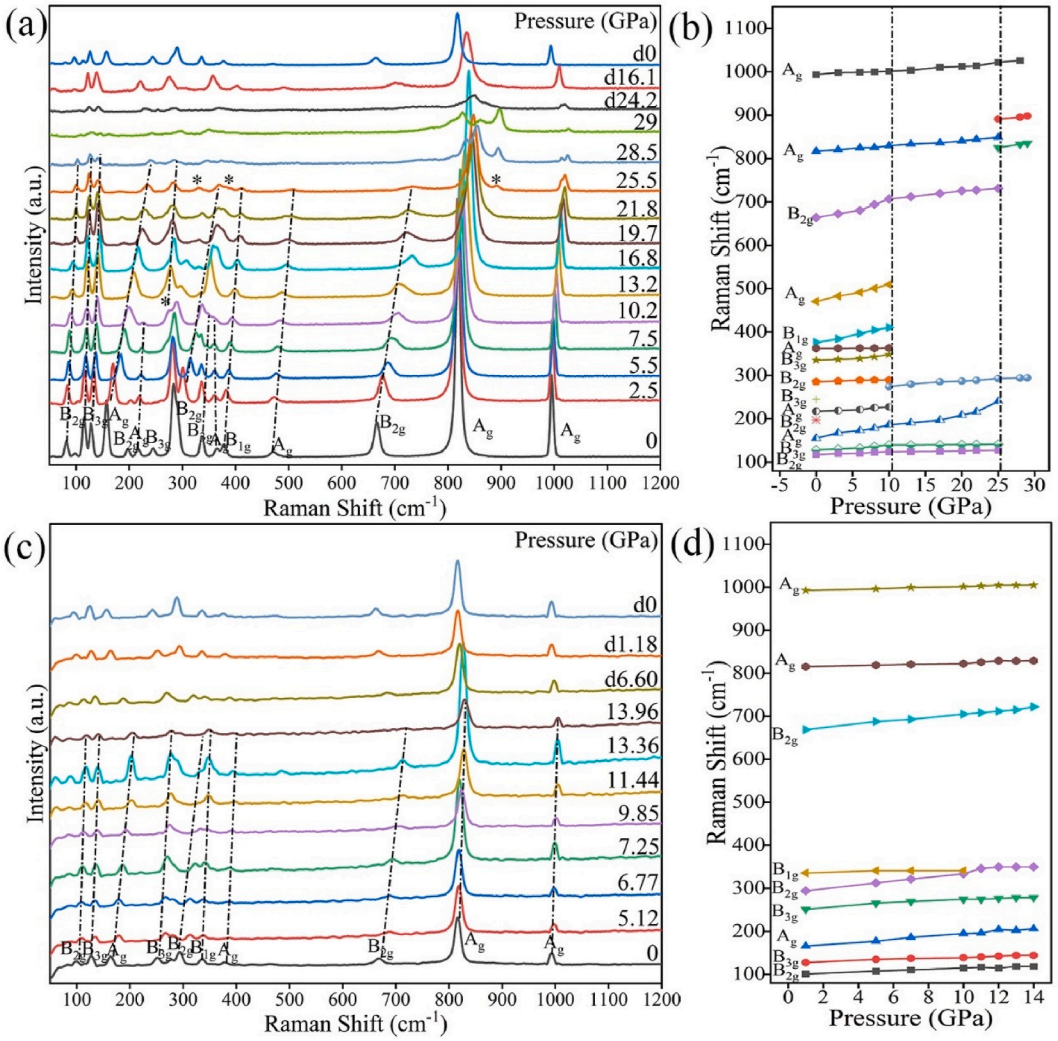

Fig. 2. (a) In situ Raman spectra of 0–29 GPa, the distribution of experimentally observed Raman peaks is based on theoretical analysis, and the symbols * represent emerging Raman peaks. (b) Pressure dependence of Raman modes derived from Fig. 2(a). (c) In situ Raman spectra of MoO_3-II at 0–14 GPa. (d) Pressure dependence of Raman modes derived from Fig. 2(c).

under the pressure of 29.5 GPa, and the optical absorption in the ultraviolet region of the sample was reduced during the decompression process, and a "bulge" appeared at 700–800 nm, which increased the absorption value of the sample. At 700–800 nm, there is a "bulge" and the absorption value increases, which may be due to the formation of defects in the quenched sample. On this phenomenon, we further investigated whether the repeated compression would have other effects on the optical absorption of MoO_3. Using the sample retained from the previous photo absorption, we performed UV–visible absorption spectroscopic characterization at pressures up to 16 GPa, and the results are shown in Fig. 3b. During the second compression-decompression process, the UV–visible spectroscopy is unchanged, except from the gradual rise.

The optical bandgap of α-MoO_3 at ambient pressure is 3.13 eV as derived from Tauc-plot (Fig. S4). As shown in Fig. 3c, with increasing pressure, the optical bandgap of MoO_3 decreases abruptly at ~11 GPa and 25 GPa, corresponding to the phase transitions. After the first compression-decompression processes, the optical bandgap of MoO_3 decreases irreversibly from 3.13 eV (α-MoO_3) to 2.40 eV (MoO_3-II) at ambient pressure and remains unchanged after the second pressure treatment, which are also consistent with UV–visible spectroscopy results and the color characteristics of the samples. As shown in Fig. 3d, the color of MoO_3 gradually deepens from the nearly transparent color at ambient pressure to deep red at high pressure, and the edge of the sample shows light green. The color further changes to black after decompression, and the color remains unchanged after recompression, which is an irreversible change. The enhanced light absorption of MoO_3 in the infrared region may indicate an interesting phenomenon, which also provides a direction for future research.

In order to understand the experimental findings, we have done XPS characterization of both MoO_3 samples and calculated the energy band structure of MoO_3 at different pressure by first-principle calculations, as shown in Fig. 4. Fig. 4a and b shows the binding energy of the photoelectron peaks of Mo3d and O1s, respectively, (see Fig. S5 for the complete XPS spectral peaks). The spectra shows that the two main peaks of Mo3d of the starting sample are located at 236.2 eV and 233.1 eV at ambient pressure, while the binding energy decreased by ~0.3 eV after pressure treatment (quenched from ~30 GPa). The binding energy of the main peaks of O1s of the starting sample is 531.0 eV, and the binding energy decreased by 0.4 eV after pressure treatment. The valence band of MoO_3 is shown in Fig. 4c. Compared with the starting sample, the valence-band maximum of the quenched sample increased by ~0.9 eV, touching the Fermi level, which indicates that the quenched sample may have metallic behavior. This phenomenon calls for further study by means of such as X-ray absorption spectroscopy (XAS), electron paramagnetic resonance (EPR), and electric resistive measurements.

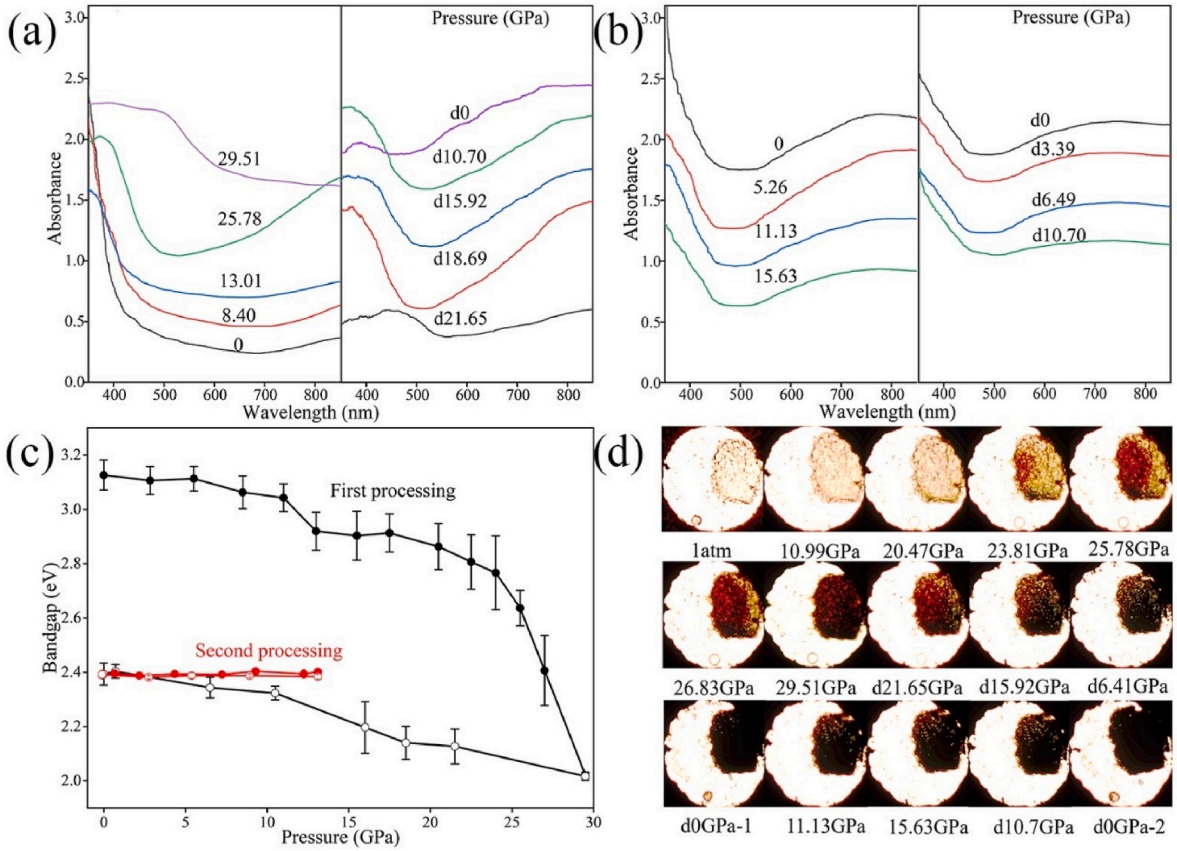

Fig. 3. (a) UV–Vis spectra of the starting α-MoO_3 upon the first compression (0–30 GPa), left: compression, right: decompression. (b) UV–Vis spectra of the quenched MoO_3-II sample upon compression (0–16 GPa), left: compression, right: decompression. (c) Optical bandgap variation plots of the two compression-decompression processes with error analysis. (d) Color change observed from microscope under pressure. (For interpretation of the references to color in this figure legend, the reader is referred to the Web version of this article.)

We calculated the energy band structures and DOS of α-MoO_3 at 1 atm (or 0 GPa) and MoO_3-II at 1 atm and 16 GPa, respectively (Fig. 4-d–g). Fig. 4d–f shows that the bandgap energy of MoO_3-II ($E_g = 1.66$ eV) is obviously lower than that of α-MoO_3 (1.97 eV) at 0 GPa, while the bandgap energy of MoO_3-II has very little change at 16 GPa (1.69 eV), consistent with above experimental results. Fig. 4g shows that the valence band is mainly contributed by the p orbitals of O atoms and the conduction band by the d orbitals of Mo atoms. In addition, other properties of MoO_3-II should be different to α-MoO_3, but to date have not been studied well. The previous calculation works show that monolayer α-MoO_3 has an ultra-low room temperature phonon thermal conductivity (κ_p) and an anisotropic infrared (IR) dielectric response [58,59], which are caused by the properties of low dimensionality of the monolayer with a few-atom-thickness [60,61], soft phonon modes [62]and strong lattice anharmonicity [63]. As mentioned above, the layered high-pressure phase MoO_3-II has a higher efficiency of layer stacking, stronger interatomic interactions and in-plane anisotropy (or lower symmetry) compared to α-MoO_3, which may lead to a different κ_p and anisotropic IR dielectric response.

We also calculated the enthalpy of α-MoO_3 and MoO_3-II. As shown in Fig. S6, the enthalpy curves of the two structures are very close and intersect at 10-12 GPa (see the inset about the enthalpy difference curves of the two phases). The calculated phase-transition pressure is in good agreement with the Raman result. When the pressure exceeds 12 GPa, the enthalpy of α-MoO_3 is larger than that of MoO_3-II, i.e., MoO_3-II is more stable than α-MoO_3, indicating the phase-transition direction from α-MoO_3 to MoO_3-II. As mentioned above, this pressure-induced phase transition involves the interlayer slipping or displacements. Generally, if there is no external force, the interlayer slipping is hard to happen. Therefore, when the pressure releases to ambient pressure, the layered high-pressure phase MoO_3-II remains stable, which is thermodynamically permitted due to the closed enthalpy values of both phases. This is the possible mechanism of the irreversible phase transition of layered MoO_3 induced by pressure. If we increase the temperature, the high-pressure phase MoO_3-II can undergo a phase transition to the low-pressure phase α-MoO_3. That is, for layered materials, the irreversible phase transition induced by pressure can be ascribed to the weak or slow kinetics of the interlayer slipping.

4. Conclusion

In conclusion, we investigated the structural evolution and irreversible changes in the optical properties of molybdenum trioxide under high pressure using high-pressure Raman spectroscopy, X-ray diffraction (XRD), UV–visible spectroscopy, and density-functional theory (DFT) calculations. In comparison to the initial low-pressure α-MoO_3 phase, the quenched MoO_3 phase displays a stabilized high-pressure phase, MoO_3-II, characterized by a narrowed bandgap (reduced by approximately 25%) and strong optical absorption within the bandgap. Importantly, the narrowing of the bandgap is irreversible. Additionally, the theoretical bandgap value of MoO_3 is in a good agreement with experimental results. These findings have significant implications for the exploration of high-pressure phase materials under ambient conditions.

CRediT authorship contribution statement

Shixia Wang: Writing – review & editing, Supervision, Investigation, Funding acquisition. **Yalin Wang:** Writing – original draft,

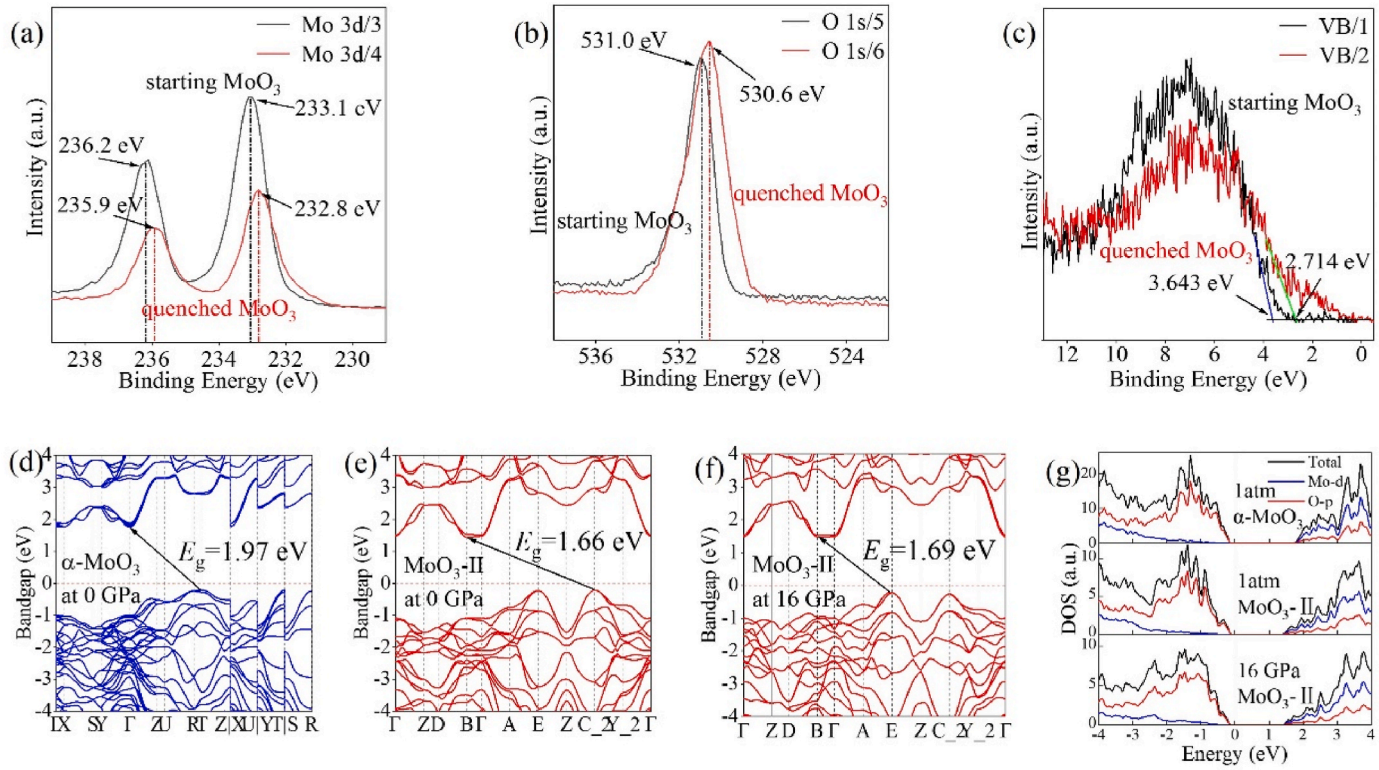

Fig. 4. XPS energy spectra of Mo3d orbitals (a), O1s orbitals (b), VB energy spectra (c) of the starting and quenched samples, respectively. First-principles calculations of electronic band structures of α-MoO_3 at 1 atm (d), MoO_3-II at 1 atm (e) and 16 GPa (f), and DOS of two structures at different pressures (g).

Investigation, Formal analysis. **Tao Liu:** Investigation, Formal analysis. **Lu Wang:** Investigation. **Yuxuan Huang:** Investigation. **Yang Lu:** Writing – review & editing, Supervision, Project administration, Investigation, Funding acquisition, Conceptualization.

Declaration of competing interest

The authors declare that they have no known competing financial interests or personal relationships that could have appeared to influence the work reported in this paper.

Data availability

Data will be made available on request.

Acknowledgements

Y.L. acknowledges the financial supports from the National Natural Science Foundation of China (NSFC, Grants No. 12204023, No. 42050203, and No. U2230401), Shanghai Science and Technology Committee, China (No. 22JC1410300) and Shanghai Key Laboratory of Material Frontiers Research in Extreme Environments, China (No. 22dz2260800). S.W. thanks the financial support from the Innovation Project of University of Shanghai for Science and Technology (Grant No. H2020341001). XRD experiments were performed at beamlines 15U1 (15U1A and 15U1B) and 17B of Shanghai Synchrotron Radiation Facility (SSRF). We thank the staffs from beamline 06 B of SSRF for assistance with IR experiments. We appreciate Dr. C.-Y. Chiang and other staffs from Taiwan Photon Source (TPS, BL21A) for helping with XRF-XAS experiments. A portion of this work (EPR) was performed on the Steady High Magnetic Field Facilities, High Magnetic Field Laboratory, CAS.

Appendix A. Supplementary data

Supplementary data to this article can be found online at https://doi.org/10.1016/j.mtadv.2024.100476.

References

[1] S. Huang, Y. Tatsumi, X. Ling, H. Guo, Z. Wang, G. Watson, A. Puretzky, A. Geohegan, D.B. Kong, J. Li, J. Yang, T. Saito, R. Dresselhaus, M. S, In-plane optical anisotropy of layered gallium telluride, ACS Nano 10 (2016) 8964, https://doi.org/10.1021/acsnano.6b05002.
[2] E. Chen, W. Xu, J. Chen, J.H. Warner, 2D layered noble metal dichalcogenides (Pt, Pd, Se, S) for electronics and energy applications, Mater. Today Advan. 7 (2020) 100076, https://doi.org/10.1016/j.mtadv.2020.100076.
[3] M. Hafeez, L. Gan, H. Li, Y. Ma, T. Zhai, Chemical vapor deposition synthesis of ultrathin hexagonal $ReSe_2$ flakes for anisotropic Raman property and optoelectronic application, Adv. Mater. 28 (2016) 8296, https://doi.org/10.1002/adma.201601977.
[4] I. Lee, J. Kim, T. Park, K. Min, Predicting mechanical properties of newly generated two-dimensional materials with minimum uncertainty, Materials Today Advances 18 (2023) 100374, https://doi.org/10.1016/j.mtadv.2023.100374.
[5] M.A. Khan, S. Yim, S. Rehman, F. Ghafoor, H. Kim, H. Patil, M.F. Khan, J. Eom, Two-dimensional materials memory devices with floating metal gate for neuromorphic applications, Materials Today Advances 20 (2023) 100438, https://doi.org/10.1016/j.mtadv.2023.100438.
[6] X. Zhou, X. Hu, S. Zhou, Q. Zhang, H. Li, T. Zhai, Ultrathin 2D $GeSe_2$ rhombic flakes with high anisotropy realized by van der Waals epitaxy, Adv. Funct. Mater. 27 (2017) 1703858, https://doi.org/10.1002/adfm.201703858.
[7] R. Frisenda, G. Sanchez-Santolino, N. Papadopoulos, J. Urban, M. Baranowski, A. Surrente, D.K. Maude, M. Garcia-Hernandez, H.S.J. van der Zant, P. Plochocka, P. San-Jose, A. Castellanos-Gomez, Symmetry breakdown in franckeite: spontaneous strain, rippling, and interlayer moiré, Nano Lett. 20 (2020) 1141, https://doi.org/10.1021/acs.nanolett.9b04536.
[8] S. Guo, Y. Zhang, Y. Ge, S. Zhang, H. Zeng, H. Zhang, 2D V-V binary materials: status and challenges, Adv. Mater. 31 (2019) 1902352, https://doi.org/10.1002/adma.201902352.
[9] S. Huang, Y. Lu, F. Wang, Y. Lei, C. Song, J. Zhang, Q. Xing, C. Wang, Y. Xie, L. Mu, G. Zhang, H. Yan, B. Chen, H. Yan, Layer-dependent pressure effect on the electronic structure of 2D black phosphorus, Phys. Rev. Lett. 127 (2021) 186401, https://doi.org/10.1103/PhysRevLett.127.186401.
[10] H. Yuan, X. Liu, F. Afshinmanesh, W. Li, G. Xu, J. Sun, B. Lian, A.G. Curto, G. Ye, Y. Hikita, Z. Shen, S.-C. Zhang, X. Chen, M. Brongersma, H.Y. Hwang, Y. Cui, Polarization-sensitive broadband photodetector using a black phosphorus vertical

p–n junction, Nat. Nanotechnol. 10 (2015) 707, https://doi.org/10.1038/nnano.2015.112.
[11] X. Wang, Y. Li, L. Huang, X.-W. Jiang, L. Jiang, H. Dong, Z. Wei, J. Li, W. Hu, Short-wave near-infrared linear dichroism of two-dimensional germanium selenide, J. Am. Chem. Soc. 139 (2017) 14976, https://doi.org/10.1021/jacs.7b06314.
[12] C. Gong, Y. Zhang, W. Chen, J. Chu, T. Lei, J. Pu, L. Dai, C. Wu, Y. Cheng, T. Zhai, L. Li, J. Xiong, Electronic and optoelectronic applications based on 2D novel anisotropic transition metal dichalcogenides, Adv. Sci. 4 (2017) 1700231, https://doi.org/10.1002/advs.201700231.
[13] S. Balendhran, J. Deng, J.Z. Ou, S. Walia, J. Scott, J. Tang, K.L. Wang, M.R. Field, S. Russo, S. Zhuiykov, M. Strano, S. Medhekar, N. Sriram, S. Bhaskaran, K. M. Kalantar-zadeh, Enhanced charge carrier mobility in two-dimensional high dielectric molybdenum oxide, Adv. Mater. 25 (2013) 109, https://doi.org/10.1002/adma.201203346.
[14] I.A. de Castro, R.S. Datta, J.Z. Ou, A. Castellanos-Gomez, S. Sriram, T. Daeneke, K. Kalantar-zadeh, Molybdenum oxides–from fundamentals to functionality, Adv. Mater. 29 (2017) 1701619, https://doi.org/10.1002/adma.201701619.
[15] s balendhran, s walia, h nili, j. z ou, s zhuiykov, r. b kaner, s sriram, m bhaskaran, k. kalantarzadeh, Two-dimensional molybdenum trioxide and dichalcogenides, Adv. Funct. Mater. 23 (2013), https://doi.org/10.1002/adfm.201300125, 3952.0.
[16] A. Arash, S.A. Tawfik, M.J.S. Spencer, S. Kumar Jain, S. Arash, A. Mazumder, E. Mayes, F. Rahman, M. Singh, V. Bansal, S. Sriram, S. Walia, M. Bhaskaran, S. Balendhran, Electrically activated UV-A filters based on electrochromic MoO_{3-x}, ACS Appl. Mater. Interfaces 12 (2020) 16997, https://doi.org/10.1021/acsami.9b20916.
[17] S. Abedini Dereshgi, T.G. Folland, A.A. Murthy, X. Song, I. Tanriover, V.P. Dravid, J.D. Caldwell, K. Aydin, Lithography-free IR polarization converters via orthogonal in-plane phonons in α-MoO_3 flakes, Nat. Commun. 11 (2020) 5771, https://doi.org/10.1038/s41467-020-19499-x.
[18] E. Cho, S. Cha, Y. Kim, C. Kim, Transparent and flexible electrode composed of a graphene multilayer interlayer-doped with MoO_3, Org. Electron. 77 (2020) 105437, https://doi.org/10.1016/j.orgel.2019.105437.
[19] W.-B. Zhang, Q. Qu, K. Lai, High-mobility transport anisotropy in few-layer MoO_3 and its origin, ACS Appl. Mater. Interfaces 9 (2017) 1702, https://doi.org/10.1021/acsami.6b14255.
[20] W. Ma, P. Alonso-González, S. Li, A.Y. Nikitin, J. Yuan, J. Martín-Sánchez, J. Taboada-Gutiérrez, I. Amenabar, P. Li, S. Vélez, C. Tollan, Z. Dai, Y. Zhang, S. Sriram, K. Kalantar-Zadeh, S.-T. Lee, R. Hillenbrand, Q. Bao, In-plane anisotropic and ultra-low-loss polaritons in a natural van der Waals crystal, Nature 562 (2018) 557, https://doi.org/10.1038/s41586-018-0618-9.
[21] Z. Zheng, N. Xu, S.L. Oscurato, M. Tamagnone, F. Sun, Y. Jiang, Y. Ke, J. Chen, W. Huang, W.L. Wilson, A. Ambrosio, S. Deng, H. Chen, A mid-infrared biaxial hyperbolic van der Waals crystal, Sci. Adv. 5 (2019) eaav8690, https://doi.org/10.1126/sciadv.aav8690.
[22] M. Chen, X. Lin, T.H. Dinh, Z. Zheng, J. Shen, Q. Ma, H. Chen, P. Jarillo-Herrero, S. Dai, Configurable phonon polaritons in twisted α-MoO_3, Nat. Mater. 19 (2020) 1307, https://doi.org/10.1038/s41563-020-0781-x.
[23] Z. Zheng, F. Sun, W. Huang, J. Jiang, R. Zhan, Y. Ke, H. Chen, S. Deng, Phonon polaritons in twisted double-layers of hyperbolic van der Waals crystals, Nano Lett. 20 (2020) 5301, https://doi.org/10.1021/acs.nanolett.0c01627.
[24] B. Zou, X. Wang, Y. Zhou, Y. Zhou, Y. Wu, T. Xing, Y. He, J. Yang, Y. Chen, P. Ren, H. Sun, Optical effect modulation in polarized Raman spectroscopy of transparent layered α-MoO_3, Small 19 (2023) 2206932, https://doi.org/10.1002/smll.202206932.
[25] Z. Zheng, J. Chen, Y. Wang, X. Wang, X. Chen, P. Liu, J. Xu, W. Xie, H. Chen, S. Deng, N. Xu, Highly confined and tunable hyperbolic phonon polaritons in van der Waals semiconducting transition metal oxides, Adv. Mater. 30 (2018) 1705318, https://doi.org/10.1002/adma.201705318.
[26] T. Wang, P. Li, B. Hauer, D.N. Chigrin, T. Taubner, Optical properties of single infrared resonant circular microcavities for surface phonon polaritons, Nano Lett. 13 (2013) 5051, https://doi.org/10.1021/nl4020342.
[27] T. Low, A. Chaves, J.D. Caldwell, A. Kumar, N.X. Fang, P. Avouris, T.F. Heinz, F. Guinea, L. Martin-Moreno, F. Koppens, Polaritons in layered two-dimensional materials, Nat. Mater. 16 (2017) 182, https://doi.org/10.1038/nmat4792.
[28] D.N. Basov, Fogler, M.M. García de Abajo, F. J, Polaritons in van der Waals materials, Science 354 (2016) aag1992, https://doi.org/10.1126/science.aag1992.
[29] G. Álvarez-Pérez, T.G. Folland, I. Errea, J. Taboada-Gutiérrez, J. Duan, J. Martín-Sánchez, A.I. Tresguerres-Mata, F. Matson, J.R. Bylinkin, A. He, M. Ma, W. Bao, Q. Martín, J.I. Caldwell, J.D. Nikitin, A. Y, P. Alonso-González, Infrared Permittivity of the biaxial van der Waals semiconductor α-MoO_3 from near- and Far-Field correlative studies, Adv. Mater. 32 (2020) 1908176, https://doi.org/10.1002/adma.201908176.
[30] K.S. Novoselov, A. Mishchenko, A. Carvalho, A.H.C. Neto, 2D materials and van der Waals heterostructures, Science 353 (2016) 6298, https://doi.org/10.1126/science.aac9439.
[31] R. Ribeiro-Palau, C. Zhang, K. Watanabe, T. Taniguchi, J. Hone, C. Dean, Twistable electronics with dynamically rotatable heterostructures, Science 361 (2018) 690, https://doi.org/10.1126/science.aat6981.
[32] G. Hu, Q. Ou, G. Si, Y. Wu, J. Wu, Z. Dai, A. Krasnok, Y. Mazor, Q. Zhang, Q. Bao, C.-W. Qiu, A. Alù, Topological polaritons and photonic magic angles in twisted α-MoO_3 bilayers, Nature 582 (2020) 209, https://doi.org/10.1038/s41586-020-2359-9.
[33] L.A. Ponomarenko, R.V. Gorbachev, G.L. Yu, D.C. Elias, R. Jalil, A.A. Patel, A. Mishchenko, A.S. Mayorov, C.R. Woods, J.R. Wallbank, M. Mucha-Kruczynski, B.A. Piot, M. Potemski, I.V. Grigorieva, K.S. Novoselov, f guinea, V.I. Fal'ko, A. K. Geim, Cloning of Dirac fermions in graphene superlattices, Nature 497 (2013) 594, https://doi.org/10.1038/nature12187.
[34] D. Kim, J. Pandey, J. Jeong, W. Cho, S. Lee, S. Cho, H. Yang, Phase engineering of 2D materials, Chem.Rev. 123 (2023) 11230, https://doi.org/10.1021/acs.chemrev.3c00132.
[35] S. Sinha, H. Kim, A.W. Robertson, Preparation and application of 0D-2D nanomaterial hybrid heterostructures for energy applications, Mater. Today Advan. 12 (2021) 100169, https://doi.org/10.1016/j.mtadv.2021.100169.
[36] W. Ma, P. Alonso-González, S. Li, A.Y. Nikitin, J. Yuan, J. Martín-Sánchez, J. Taboada-Gutiérrez, I. Amenabar, P. Li, S. Vélez, C. Tollan, Z. Dai, Y. Zhang, S. Sriram, K. Kalantar-Zadeh, S.-T. Lee, R. Hillenbrand, Q. Bao, In-plane anisotropic and ultra-low-loss polaritons in a natural van der Waals crystal, Nature 562 (2018) 557, https://doi.org/10.1038/s41586-018-0618-9.
[39] V. Kumar, A. Sumboja, J. Wang, V. Bhavanasi, V.C. Nguyen, P.S. Lee, Topotactic phase transformation of hexagonal MoO3 to layered MoO3-II and Its two-dimensional (2D) nanosheets, Chem. Mater. 26 (2014) 5533–5539, https://doi.org/10.1021/cm502558t.
[41] V. Kumar, L. Liu, V.C. Nguyen, V. Bhavanasi, K. Parida, D. Mandler, P.S. Lee, Localized charge transfer in two-dimensional molybdenum trioxide, ACS Appl. Mater. Interfaces 9 (2017) 27045, https://doi.org/10.1021/acsami.7b09641.
[42] H. Kim, J.H. Kim, J. Kim, J. Park, K. Park, J.-H. Baek, J.-C. Shin, H. Lee, J. Son, S. Ryu, Y.-W. Son, H. Cheong, G.-H. Lee, In-plane anisotropy of graphene by strong interlayer interactions with van der Waals epitaxially grown MoO_3, Sci. Adv. 9 (2023) eadg6696, https://doi.org/10.1126/sciadv.adg6696.
[44] T. Akamatsu, T. Ideue, L. Zhou, Y. Dong, S. Kitamura, M. Yoshii, D. Yang, M. Onga, Y. Nakagawa, K. Watanabe, T. Taniguchi, J. Laurienzo, J. Huang, Z. Ye, T. Morimoto, H. Yuan, Y. Iwasa, A van der Waals interface that creates in-plane polarization and a spontaneous photovoltaic effect, Science 372 (2021) 68, https://doi.org/10.1126/science.aaz9146.
[45] H.K. Mao, J. Xu, P.M. Bell, Calibration of the ruby pressure gauge to 800 kbar under quasi-hydrostatic conditions, J. Geophys. Res. Solid Earth 91 (1986) 4673, https://doi.org/10.1029/JB091iB05p04673.
[46] Y. Lu, H. Yan, E. Huang, B. Chen, Persistent negative compressibility coupled to optical modulation in empty-perovskite $TiOF_2$, J. Phys. Chem. C 125 (2021) 8869, https://doi.org/10.1021/acs.jpcc.1c01601.
[47] J.P. Perdew, K. Burke, M. Ernzerhof, Generalized gradient approximation made simple, Phys. Rev. Lett. 77 (1996) 3865, https://doi.org/10.1103/PhysRevLett.77.3865.
[48] S. Grimme, J. Antony, S. Ehrlich, H. Krieg, A consistent and accurate ab initio parametrization of density functional dispersion correction (DFT-D) for the 94 elements H-Pu, J. Chem. Phys. 132 (2010). http://10.1063/1.3382344.
[49] V. Wang, N. Xu, J.-C. Liu, G. Tang, W.-T. Geng, VASPKIT: a user-friendly interface facilitating high-throughput computing and analysis using VASP code, Comput. Phys. Commun. 267 (2021). http://10.1016/j.cpc.2021.108033.
[50] Z. Wang, Y. Wang, J. Wang, Y. Song, M.J. Robson, A. Seong, M. Yang, Z. Zhang, A. Belotti, J. Liu, G. Kim, J. Lim, Z. Shao, F. Ciucci, Rational design of perovskite ferrites as high-performance proton-conducting fuel cell cathodes, Nat. Catal. 5 (2022) 777, https://doi.org/10.1038/s41929-022-00829-9.
[51] F. Li, X. Deng, Z. Shi, S. Wu, Z. Zeng, D. Wang, Y. Li, F. Qi, Z. Zhang, Z. Yang, S.-H. Jang, F.R. Lin, S.W. Tsang, X.-K. Chen, A.K.Y. Jen, Hydrogen-bond-bridged intermediate for perovskite solar cells with enhanced efficiency and stability, Nat. Photonics 17 (2023) 478, https://doi.org/10.1038/s41566-023-01180-6.
[52] Y. Zhao, C. Deng, D. Tang, L. Ding, Y. Zhang, H. Sheng, H. Ji, W. Song, W. Ma, C. Chen, J. Zhao, α-Fe_2O_3 as a versatile and efficient oxygen atom transfer catalyst in combination with H_2O as the oxygen source, Nat. Catal. 4 (2021) 684, https://doi.org/10.1038/s41929-021-00659-1.
[53] D. Liu, W.W. Lei, J. Hao, D. Liu, B. D.Liu, B. Wang, X. Chen, X.H. Cui, Q.L. Zou, G. T. Liu, S. J.Jiang, High-pressure Raman scattering and x-ray diffraction of phase transitions in MoO_3, J. Appl. Phys. 105 (2009) 023513, https://doi.org/10.1063/1.3056049.
[54] E.M. McCarron, J.C. Calabrese, The growth and single crystal structure of a high pressure phase of molybdenum trioxide: MoO_3-II, J. Solid State Chem. 91 (1991) 121, https://doi.org/10.1016/0022-4596(91)90064-O.
[55] S. Duwal, M. Kim, S. Kawaguchi, N. Hirao, Y. Ohishi, C.-S. Yoo, Phase transitions and resistivity anomaly of layered MoO_3 at high pressure, J. Phys. Chem. C 122 (2018) 22632, https://doi.org/10.1021/acs.jpcc.8b06434.
[56] S. Phadungdhitidhada, P. Mangkorntong, S. Choopun, N. Mangkorntong, Raman scattering and electrical conductivity of nitrogen implanted MoO_3 whiskers, Ceram. Int. 34 (2008) 1121, https://doi.org/10.1016/j.ceramint.2007.09.093.
[57] M. Dieterle, G. Mestl, Raman spectroscopy of molybdenum oxides Part II. Resonance Raman spectroscopic characterization of the molybdenum oxides Mo_4O_{11} and MoO_2, Phys. Chem. Chem. Phys. 4 (2002) 822, https://doi.org/10.1039/B107046K.
[58] Z. Tong, T. Dumitrică, T. Frauenheim, Ultralow thermal conductivity in two-dimensional MoO_3, Nano Lett. 21 (2021) 4351, https://doi.org/10.1021/acs.nanolett.1c00935.
[59] Z. Tong, T. Dumitrică, T. Frauenheim, First-principles prediction of infrared phonon and dielectric function in biaxial hyperbolic van der Waals crystal α-MoO_3, Phys. Chem. Chem. Phys. 23 (2021) 19627, https://doi.org/10.1039/D1CP00682G.
[60] H. Xie, M. Hu, H. Bao, Thermal conductivity of silicene from first-principles, Appl. Phys. Lett. 104 (2014), https://doi.org/10.1063/1.4870586.

[61] Z. Gao, F. Tao, J. Ren, Unusually low thermal conductivity of atomically thin 2D tellurium, Nanoscale 10 (2018) 12997, https://doi.org/10.1039/C8NR01649F.
[62] A. Jain, A.J.H. McGaughey, Strongly anisotropic in-plane thermal transport in single-layer black phosphorene, Sci. Rep. 5 (2015) 8501, https://doi.org/10.1038/srep08501.
[63] G. Qin, Z. Qin, W.-Z. Fang, L.-C. Zhang, S.-Y. Yue, Q.-B. Yan, M. Hu, G. Su, Diverse anisotropy of phonon transport in two-dimensional group IV–VI compounds: a comparative study, Nanoscale 8 (2016) 11306, https://doi.org/10.1039/C6NR01349J.